




Disorder-induced phase transitions in double Weyl semimetals

Jiayan Zhang, Fei Wan, Xinru Wang, Ying Ding, Liehong Liao , Zhihui Chen, M. N. Chen,^{*} and Yuan Li [†]
Department of Physics, Hangzhou Dianzi University, Hangzhou, Zhejiang 310018, China

 (Received 11 June 2022; revised 18 September 2022; accepted 25 October 2022; published 4 November 2022)

The double Weyl semimetal (DWSM) is a newly proposed topological material that hosts Weyl points with chiral charge $n = 2$. The disorder effect in DWSM is investigated by adopting the tight-binding Hamiltonian. Using the transfer matrix method and the noncommutative Kubo formula, we numerically calculate the localization length and the Hall conductivity in the presence of the on-site nonmagnetic disorder or orbital (spin-flip) disorders, and give the corresponding global phase diagrams. For the on-site nonmagnetic disorder, the system undergoes the DWSM-3D quantum anomalous Hall (3D QAH) and normal insulator (NI)-DWSM phase transitions, and evolves into the diffusive metal phase before entering the gapless Anderson insulator phase, which is consistent with the Weyl semimetal. For σ_x orbital disorder, increasing disorder strength can generate a pair of Weyl nodes at the boundary of the Brillouin zone and induce a 3D QAH-DWSM phase transition. Surprisingly, DOS calculations manifest that the insulator phase induced by the σ_x disorder is gapped, which is different from the gapless DOS in the system with σ_0 disorders. Another difference is the direct DWSM-NI transition. These results indicate that the σ_0 and σ_x disorders have a diverse impact on the system. Then we investigate the interplay of orbital disorders for both disordered 3D QAH phase and DWSM phase. The disorder-induced transitions at low disorders can be well understood in terms of the self-consistent Born approximation.

DOI: [10.1103/PhysRevB.106.184202](https://doi.org/10.1103/PhysRevB.106.184202)

I. INTRODUCTION

The Weyl semimetal is a three-dimensional topological state of matter, in which the conduction and valence bands touch at a finite number of nodes [1–3]. The Weyl nodes always appear in pairs and each Weyl node can be regarded as a monopole in k space carrying the chiral charge $n = 1$. The Weyl semimetal has the Fermi arc surface states that connect the surface projections of two Weyl nodes [4]. The Weyl semimetal has been predicted to exist in many materials [4–9]. Researchers found the Weyl fermions in TaAs [10], ferromagnetic semimetal $\text{Co}_3\text{Sn}_2\text{S}_2$ [11], and MoTe_2 [12]. The Weyl semimetal supports many fascinating properties such as the chiral anomaly [13–17], quantum Hall effect [18–20], anomalous Hall effect [21,22], the nonlinear optical effect [23,24], and the magneto-optical response [25,26].

However, the chiral charge of the Weyl node can be more than one, namely $n > 1$, and the corresponding materials are named as multi-Weyl semimetals [27–30]. For $n = 2$, which is the double Weyl semimetal (DWSM), the dispersion relation in the vicinity of such node is quadratic in two directions and linear in the third direction. These Weyl nodes are protected by the crystallographic point group symmetries [27]. The DWSM is theoretically proposed in HgCr_2Se_4 [6] and SrSi_2 [28] and can be achieved in photonic crystals [29]. Numerical calculations suggest the presence of multiple surface Fermi arcs in multi-Weyl semimetals [31–33]. The topological

semimetal with a large chiral charge can also induce intriguing transport phenomena [30].

Quantum interference can completely suppress the diffusion of a particle in a random potential, a phenomenon known as Anderson localization [34]. Li *et al.* investigated the role of disorder in the HgTe/CdTe quantum well and found, surprisingly, that disorder can induce the topological phase transition and generate the topological Anderson insulator phase [35]. Afterward, the disorder effect was extensively discussed in 3D topological insulators [36], the Kane-Mele model [37], the HgTe/CdTe quantum well [38,39], Dirac semimetal thin films [40], quasicrystals [41,42], Weyl semimetals [43–48], and higher-order topological materials [49,50]. The disorder can also induce phase transitions between type-I and type-II Weyl semimetals [51]. However, the role of disorder in the DWSM has not been thoroughly investigated and needs to be further explored. Besides, most of the works only involve the on-site nonmagnetic disorder referring to the σ_0 term in the Hamiltonian. There also exists the bond disorder [52–55], the orbital disorder or spin-flip disorder referring to σ_x , σ_y , or σ_z terms in the Hamiltonian. The orbital (or spin-flip) disorder can also alter the topological properties of various systems [47,56,57]. In addition, the effect of the orbital (or spin-flip) disorder in the DWSM has not been discussed yet.

In this paper, we first study the effect of the on-site nonmagnetic and orbital (or spin-flip) disorders in the DWSM by calculating the localization length and the Hall conductivity. These disorders can give rise to rich phase transitions shown in the phase diagrams. First, the tight-binding Hamiltonian of the DWSM is introduced in momentum and real space. Then the phase diagram in the clean limit is presented. In the

^{*}mnchen@hdu.edu.cn

[†]liyuan@hdu.edu.cn

presence of disorder, the results indicate that the 3D quantum anomalous Hall (3D QAH) phase and DWSM phase are stable in the weak disorder and the system undergoes a series of phase transitions with increasing of the disorder strength. For nonmagnetic disorder, phase transitions in the DWSM are consistent with those reported in the Weyl semimetal [43,58]. We calculate the density of states (DOS) for different disorder strengths. For the σ_x orbital (or spin-flip) disorder, the 3D QAH–DWSM transition is consistent with that reported in the previous research [47]. However, according to the DOS calculation, the system enters into a gapped insulator phase instead of the gapless Anderson insulator (AI) phase generated by σ_0 disorder. Another difference is the direct transition from DWSM to normal insulator (NI) phase, which is also different from the effect of the σ_0 disorder. For the latter, the system must enter the diffusive metal (DM) phase before being localized by the strong disorder. The combined effect of orbital disorders is also investigated for disordered 3D QAH and DWSM phases. Furthermore, the self-consistent Born approximation (SCBA) is introduced to explain the disorder-induced phase transitions. At last, we discuss the experimental realization of the disordered DWSM.

The paper is organized as follows: In Sec. II, we introduce the model Hamiltonian and give the phase diagram in the clean limit. The numerical calculation methods are also given here. In Sec. III, we show the localization length and Hall conductivity and plot the global phase diagrams and DOS in the presence of disorder. In Sec. IV, we interpret the disorder effect in terms of the SCBA method. Finally, a brief discussion and summary are given in Sec. V.

II. MODEL AND METHOD

We consider the tight-binding Hamiltonian that describes the DWSM on a simple cube lattice with the lattice constant $a \equiv 1$. The Hamiltonian has the form [32,47]

$$h(\mathbf{k}) = t_x(\cos k_x - \cos k_y)\sigma_x + t_y \sin k_x \sin k_y \sigma_y + (m_z - \cos k_x - \cos k_y - t_z \cos k_z)\sigma_z, \quad (1)$$

where $t_{x,y,z}$ and m_z are model parameters. $\sigma_{x,y,z}$ are Pauli matrices in the orbital (or spin) space. The Hamiltonian (1) has the form of $h(\mathbf{k}) = \mathbf{d}(\mathbf{k}) \cdot \boldsymbol{\sigma}$. Diagonalizing the Hamiltonian (1), we can get the energy spectrum $E_k = \pm \sqrt{d_x^2(\mathbf{k}) + d_y^2(\mathbf{k}) + d_z^2(\mathbf{k})}$. The conduction and valence bands touch each other when $d_x(\mathbf{k}) = d_y(\mathbf{k}) = d_z(\mathbf{k}) = 0$. By solving the equations, we can obtain a pair of twofold degenerate double Weyl points [see Figs. 1(c) and 1(d)] located at $(0, 0, \pm \arccos[(m_z - 2)/t_z])$ for $2 - t_z < m_z < 2 + t_z$. When $t_z - 2 < m_z < 2 - t_z$, the energy spectrums open a topological nontrivial gap and this model corresponds to the 3D QAH phase [see Fig. 1(b)]. When $m_z > 2 + t_z$, the spectrums open a gap as well but the model now is topologically trivial and generates a NI phase. According to the above inequality equations, we draw the phase diagram in the clean limit in Fig. 1(a). In this work, we choose $t_z = 0.5$ and $t_x = t_y = 1$.

It is not convenient to include the disorder effect in Eq. (1) in k space, so we take the Fourier transform

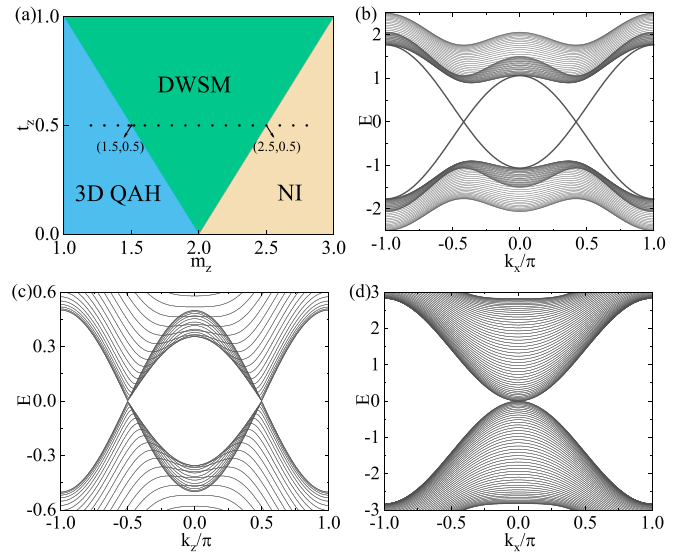


FIG. 1. (a) Phase diagram of DWSM without disorder on the t_z - m_z plane. There are 3D QAH, DWSM, and NI phases for different m_z . (b) Band structure of 3D QAH phase with open boundary condition in the y direction ($N_y = 50$) for $k_z = 0$ and $m_z = 1$. (c) Band structure on the E - k_z plane with $k_x = k_y = 0$ and $m_z = 2$. The Weyl nodes are located at $(0, 0, \pm\pi/2)$. (d) Band structure on the E - k_x plane with $k_y = 0$, $k_z = \pi/2$, and $m_z = 2$. The dispersion relation is quadratic in the k_x direction near the Weyl node. Other parameters are $t_x = t_y = 1$.

$a_{k\sigma} = (1/\sqrt{V}) \sum_r e^{ikr} a_{r\sigma}$ and get the real-space Hamiltonian

$$H_{\text{real}} = \sum_r a_r^\dagger T_0 a_r + (a_{r+x}^\dagger T_x a_r + a_{r+y}^\dagger T_y a_r + a_{r+z}^\dagger T_z a_r + a_{r+x+y}^\dagger T_{xy1} a_r + a_{r+x-y}^\dagger T_{xy2} a_r + \text{H.c.}), \quad (2)$$

where $a_r^\dagger = (a_{r\sigma}^\dagger, a_{r\sigma'})^\dagger$ with $a_{r\sigma}^\dagger$ ($a_{r\sigma}$) being the creation (annihilation) operator at site \mathbf{r} for the electron with σ , and x, y, z denote the hopping directions. T_0 is the on-site energy; T_x, T_y , and T_z are the nearest-neighbor hopping matrices along the x, y, z axis. T_{xy1} (T_{xy2}) is the next-nearest-neighbor hopping matrix along the $\mathbf{x} + \mathbf{y}$ ($\mathbf{x} - \mathbf{y}$) direction. Here $T_0 = m_z \sigma_z$, $T_x = \frac{1}{2}(\sigma_x - \sigma_z)$, $T_y = -\frac{1}{2}(\sigma_x + \sigma_z)$, $T_z = -\frac{1}{2}t_z \sigma_z$, $T_{xy1} = -\frac{1}{4}\sigma_y$, and $T_{xy2} = \frac{1}{4}\sigma_y$.

The orbital (or spin-flip) disorder can be introduced by adding the random Hamiltonian H_{disorder} [47,59] to Eq. (2) to calculate the localization length and DOS:

$$H_{\text{disorder}} = \sum_{(\mathbf{r}, \mathbf{r}')} a_r^\dagger [U_x^r \sigma_x + U_y^r \sigma_y + U_z^r \sigma_z + U_0^r \sigma_0] a_{r'}. \quad (3)$$

For $\mathbf{r} \neq \mathbf{r}'$, this Hamiltonian means that the hopping term between neighboring sites is random and this disorder is termed as bond disorder [52,53]. When $\mathbf{r} = \mathbf{r}'$ (only summation over the variation \mathbf{r}), the Hamiltonian can describe the orbital disorder or the spin-flip disorder. In this article, we only study the case of $\mathbf{r} = \mathbf{r}'$. The first three terms denote the orbital (or spin-flip) disorder and the last term is the on-site nonmagnetic disorder. $U_{x,y,z,0}^r$ are uniformly distributed within $[-W_{x,y,z,0}/2, W_{x,y,z,0}/2]$ with $W_{x,y,z,0}$ representing the disorder strength.

We use the transfer matrix method to numerically calculate the localization length to determine the phase boundary induced by disorder [60–64]. We consider a quasi-one-dimensional long bar with the system volume $L_x \times L_y \times L_z$ and apply periodic boundary conditions in the x and y directions. We divide the system into slices with each slice's cross section $L_x \times L_y = L \times L$. We let ψ_n and $H_{n,n}$ be the wave function and hopping matrix of the n th slice. $H_{n,n-1}$ ($H_{n,n+1}$) is the hopping matrix between the n th and $(n-1)$ th [$(n+1)$ th] slice. The Schrödinger equation can be written as [47,60]

$$H_{n,n}\psi_n + H_{n,n+1}\psi_{n+1} + H_{n,n-1}\psi_{n-1} = E\psi_n. \quad (4)$$

Equation (4) can be further expressed as

$$\begin{pmatrix} \psi_{n+1} \\ \psi_n \end{pmatrix} = T_n \begin{pmatrix} \psi_n \\ \psi_{n-1} \end{pmatrix}, \quad (5)$$

with the transfer matrix

$$T_n = \begin{pmatrix} H_{n,n+1}^{-1}(E - H_{n,n}) & -H_{n,n+1}^{-1}H_{n,n-1} \\ 1 & 0 \end{pmatrix}. \quad (6)$$

$Q_{L_z} = \prod_{n=1}^{L_z} T_n$ is the product of the transfer matrix and there exists a limit matrix $\Gamma = \lim_{L_z \rightarrow +\infty} (Q_{L_z}^\dagger Q_{L_z})^{\frac{1}{2L_z}}$. By diagonalizing the matrix Γ , we obtain the normalized eigenvectors $\{u_i\}$. The Lyapunov exponent is defined as

$$\gamma_i = \frac{1}{L_z} \lim_{L_z \rightarrow +\infty} \ln \|Q_{L_z} u_i\|. \quad (7)$$

The localization length λ characterizes the largest possible extension of a state and is defined as the inverse of the smallest positive γ_i by $\lambda = 1/\gamma_{\min}$. Besides, to determine the critical point of the phase transition, what we need is the normalized localization length Λ defined as $\Lambda = \lambda/L$, where L is the side length of each slice. In the following calculation, we choose $L = 8, 10, 12$, and 14 ignoring the unit since we fix the lattice constant to be $a \equiv 1$. In general, in the metallic phase, the rate of change of normalized localization length Λ with the system size L satisfies $d\Lambda/dL > 0$. In the insulator phase, $d\Lambda/dL < 0$. A phase transition happens when $d\Lambda/dL = 0$.

In the clean limit, we can view the DWSM as coupled multiple 2D subsystems labeled by k_z as $H_0(k_z)$ [65]. The Weyl nodes are located at $(0, 0, \pm k_0)$. For $k_z \in (-k_0, k_0)$, the subsystem is a 2D Chern insulator and contributes a quantized Hall conductance $\sigma_{xy}^{2D} = 2e^2/h$. For $k_z \notin (-k_0, k_0)$, the system is topologically trivial and therefore has no contribution to the Hall conductance. The total Hall conductivity of the 3D system is $\sigma_{xy}^{3D} = \sum_{k_z} \sigma_{xy}^{2D}(k_z)/L_z$ with L_z being the size along the z direction. In the presence of disorder, the Hall conductivity can be calculated by the noncommutative geometry method [66–69], which is used to calculate the Chern number in real space now that the disorder can break the translational symmetry in k space. When calculating the disorder-induced Chern number, we adopted an approximation that there still exists a translational symmetry along the z direction in the presence of disorder [58,70]. In terms of this approximation, we can get the Hall conductivity by calculating the k_z -dependent Chern number for all of the 2D planes and summing them together, which vastly saves computing time compared to the direct diagonalization of the 3D Hamiltonian

[50]. The Chern number in real space can be expressed as

$$C = -\frac{2\pi i}{N^2} \left\langle \sum_{n,\alpha} \langle n, \alpha | P[-i[x_1, P], -i[x_2, P]] | n, \alpha \rangle \right\rangle_W, \quad (8)$$

where

$$[x_i, P] = i \sum_{m=1}^Q c_m (e^{-imx_i \Delta_i} P e^{imx_i \Delta_i} - e^{imx_i \Delta_i} P e^{-imx_i \Delta_i}). \quad (9)$$

In Eqs. (8) and (9), N is the sample size along the x and y directions, $\Delta_i = 2\pi/N$. P is the projection operator of the occupied state in the real space and $|n, \alpha\rangle$ is the real-space coordinate. $\langle \dots \rangle_W$ represents the average over the different disorder configurations. In terms of the noncommutative geometry method, Q takes the integer between 0 and $N/2$. During the process of calculating the Chern number, one need to solve the inverse of one required matrix. For $Q \in [1, 8]$, the inverse matrix exists, but when $Q \geq 9$, the inverse matrix is close to a singular value and the numerical results might be not accurate. Thus in our calculation, we set $Q = 8$ to obtain accurate and reliable results.

III. NUMERICAL RESULTS

In this section, we numerically calculate the localization length and the Hall conductivity based on the above methods and draw the global phase diagrams in the presence of disorder. In Sec. III A and Sec. III B, we consider the nonmagnetic disorder σ_0 and the σ_x orbital disorder, respectively. In Sec. III C, we investigate the combined effect of three sorts of orbital disorders.

A. On-site nonmagnetic disorder

By adjusting the parameter m_z in Eq. (1), the system in the clean limit can be 3D QAH, DWSM, or NI phase [marked by the black dots in Fig. 1(a)] with $t_z = 0.5$ and $t_{x,y} = 1$. Here we set $m_z \in [1.2, 2.8]$ and investigate the phase transition caused by the nonmagnetic disorder. We calculate the renormalized localization length to determine the phase boundaries and the Hall conductivity to distinguish different phases. The 3D QAH phase has a quantized Hall conductivity. In the DWSM phase, the Hall conductivity is fractionally quantized. This fractionally quantized Hall conductivity is a finite-size effect. When the size in the z direction is large enough, the Hall conductivity gradually approaches the nonquantized thermodynamic limit value and the fractional plateau disappears. Figure 2 shows the phase diagram on the W_0 - m_z plane for $t_z = 0.5$ and $t_x = t_y = 1$. We can see that, with increasing of the disorder strength, the system gradually evolves from 3D QAH, DWSM, or NI phase into DM phase, and then AI phase. The dark blue lines with dots are identified by using the transfer matrix method, which are used to determine the phase boundaries. In order to verify the reliability of the phase boundary, we calculate the self-energy correction to the Hamiltonian in terms of the SCBA (see Sec. IV). The phase boundaries obtained from the SCBA are represented by the red dotted line, as shown in Fig. 2, and agree well with the results of the transfer matrix method in the case of weak

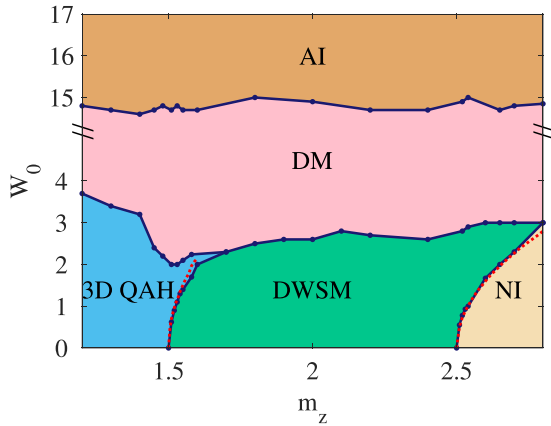


FIG. 2. Phase diagram on the W_0 - m_z plane for $t_z = 0.5$ and $t_x = t_y = 1$. The dark blue solid lines with dots are identified by using the transfer matrix method. The accurate phases are determined by the Hall conductivity σ_{xy} . The red dotted line is obtained numerically by using SCBA.

disorders. Similar numerical results obtained from the SCBA are presented in Figs. 7 and 11.

We pick four typical results of the localization length and the Hall conductivity for $m_z = 1.3, 1.52, 1.7,$ and 2.52 , and plot them in Fig. 3 and Fig. 4. For $m_z = 1.3$, the rate of change $d\Lambda/dL$ of the normalized localization length is a negative value; i.e., the Λ decreases with the increase of side length L from 8 to 12 for a fixed $W_0 < 3.4$. Meanwhile, the Hall conductivity stays quantized $\sigma_{xy} = 16e^2/8h$, which indicates that the 3D QAH phase is robust against the weak disorder. In Fig. 3(a), $d\Lambda/dL = 0$ at $W_0 = 3.4$ shows the existence of a phase transition. By increasing the disorder strength, $d\Lambda/dL$

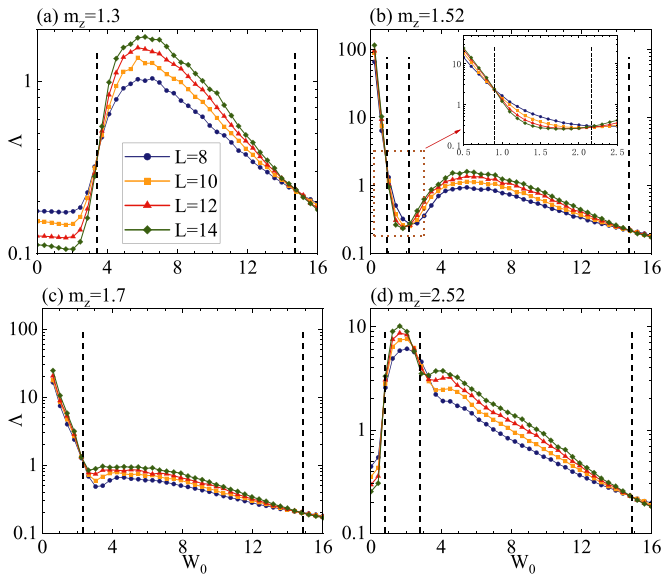


FIG. 3. The normalized localization length Λ is plotted as a function of the disorder strength W_0 for the values of (a) $m_z = 1.3$, (b) 1.52, (c) 1.7, and (d) 2.52. The inset in Fig. 3(b) shows the details near the phase transition points. Four colored curves are associated with different side lengths of the cross section. Other parameters are $t_z = 0.5$ and $t_x = t_y = 1$.

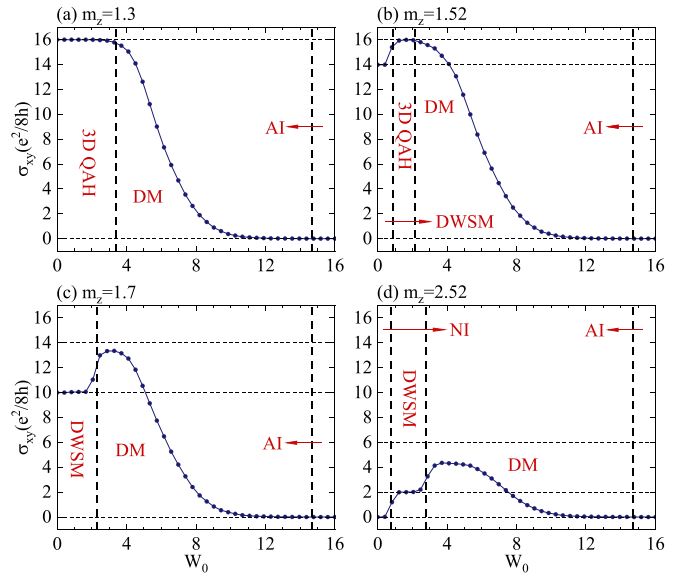


FIG. 4. The Hall conductivity σ_{xy} as a function of the disorder strength W_0 for the values of (a) $m_z = 1.3$, (b) 1.52, (c) 1.7, and (d) 2.52. The system size is $40 \times 40 \times 8$. Other parameters are $t_z = 0.5$ and $t_x = t_y = 1$.

turns to a positive value and the Hall conductivity σ_{xy} becomes nonquantized; thus the system evolves into the DM phase. In regard to the DM phase, on the one hand, the disorder destroys the surface states of 3D QAH when $W_0 > 3.4$ and therefore the quantized Hall conductivity disappears. On the other hand, the disorder can broaden the band and the broadened conduction and valence bands mix up; thus the system becomes gapless. Even though the bulk electrons experience the weak-disorder scattering, the electrons can still diffuse through the material and contribute to Hall conductivity. This Hall conductivity is nonquantized and can be expressed by the Einstein relation $\sigma = e^2 \frac{\partial n}{\partial \mu} D$ where $\frac{\partial n}{\partial \mu}$ is the DOS at the Fermi energy and D is the diffusion constant. Further increasing the disorder strength, $d\Lambda/dL$ again becomes the negative value and the second phase transition happens at $W_0 = 14.7$. The vanishing Hall conductivity $\sigma_{xy} = 0$ in Fig. 4(a) manifests that the system is localized by the strong disorder and evolves into the AI phase. For $m_z = 1.52$, a phase transition from the DWSM phase to 3D QAH phase occurs as evidenced by the Hall conductivity transition from $14e^2/8h$ to $16e^2/8h$ in Fig. 4(b) and $d\Lambda/dL$ changing from a positive to negative value in Fig. 3(b) at $W_0 = 0.9$. Based on the SCBA (see Sec. IV), the nonmagnetic disorder renormalizes the mass term m_z in the Hamiltonian (1) with m_z determining the positions of the Weyl nodes in the Brillouin zone. Utilizing the zero-order Born approximation (BA), one can qualitatively understand the phenomenon of the phase transition. According to Eq. (12), the renormalized mass term \tilde{m}_z decreases with the increase of the disorder strength W_0 , which causes a pair of Weyl nodes to depart from each other and move to the boundary of the Brillouin zone (see Fig. 5). When they arrive at the zone boundary, they annihilate pairwise and a nontrivial bulk gap arises, and the system realizes the phase transition from DWSM to 3D QAH phase. Further increasing

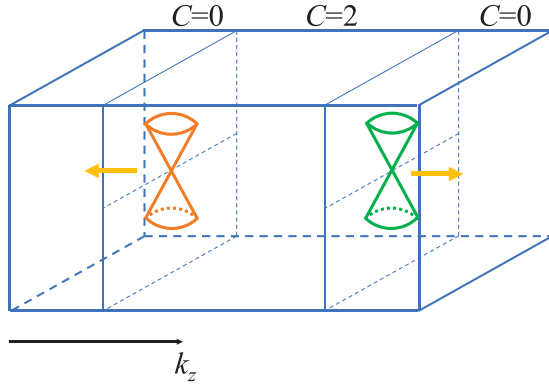


FIG. 5. The schematic diagram of the Weyl cone in the Brillouin zone. The direction of the arrow represents the direction of motion of the Weyl node. The difference of the color for the Weyl cones refers to different chirality.

the disorder strength to $W_0 = 2.16$, $d\Lambda/dL$ turns to a positive value and the Hall conductivity becomes nonquantized, which means the system evolving into the DM phase. Likewise, the system is localized when the disorder strength surpasses the value of $W_0 = 14.8$.

For $m_z = 1.7$, as shown in Figs. 3(c) and 4(c), a DWSM-DM phase transition happens at $W_0 = 2.3$ as the disorder strength increases. In this parameter configuration, the 3D QAH phase disappears compared with $m_z = 1.52$. The disappearance of the 3D QAH phase can be interpreted in terms of the SCBA. The renormalized mass term \tilde{m}_z decreases with the increase of W_0 . If \tilde{m}_z decreases to 1.5 [the phase transition point between 3D QAH and DWSM phase in Fig. 1(a)], the DWSM-3D QAH phase transition happens. For $m_z = 1.7$, the system enters the DM phase at $W_0 = 2.3$. According to the SCBA, the self-energy correction Σ_z for $W_0 = 2.3$ is -0.13 . Thus the renormalized mass term $\tilde{m}_z = m_z + \Sigma_z = 1.7 - 0.13 = 1.57$, which is greater than 1.5. Since \tilde{m}_z controls the location of Weyl nodes in BZ, the Weyl nodes are destroyed by the disorder strength at $W_0 = 2.3$ before they reach the BZ boundary. Subsequently the system undergoes the DM and AI phase. The DOS is also calculated for $m_z = 1.7$ at different disorder strengths by using the nonequilibrium Green's function (NEGF) method (see Appendix A). For $W_0 = 0$, Fig. 6(a) shows the DOS of the DWSM. When $W_0 = 4$, the Weyl nodes are destroyed and the energy bands are broadened. The DOS at $E_f = 0$ becomes finite, which means the system entering the DM phase. When W_0 increases to 16 [see Fig. 6(c)], the DOS is about 0.12 and the Hall conductivity becomes zero. It means that the electrons are localized by strong disorders and the system becomes an Anderson insulator. When the parameters are chosen as $m_z = 2.7$ and $W_0 = 0$, the DOS is zero when the Fermi energy is in the band gap, namely $-0.2 < E_f < 0.2$ eV. Correspondingly, the system is in the NI phase. For the NI phase, the zero value of the Hall conductivity arises from the vanishing DOS.

For $m_z = 2.52$, with increasing of the disorder strength, as shown in Figs. 3(d) and 4(d), a phase transition takes place at $W_0 = 0.78$ and the Hall conductivity increases from $\sigma_{xy} = 0$ to a fractional quantized value of $\sigma_{xy} = 2e^2/8h$. This interesting phase transition can also be qualitatively understood by

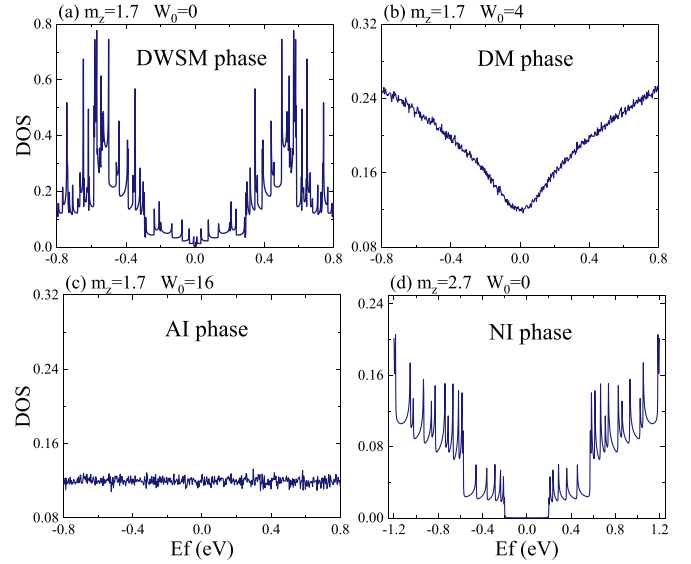


FIG. 6. DOS as a function of Fermi energy obtained by NEGF for different m_z and W_0 . $m_z = 1.7$ and (a) $W_0 = 0$ for DWSM phase, (b) $W_0 = 4$ for DM phase, (c) $W_0 = 16$ for AI phase. (d) $m_z = 2.7$ and $W_0 = 0$ for NI phase. Other parameters are $t_z = 0.5$ and $t_x = t_y = 1$.

the zero-order BA. According to Eq. (12), the renormalized mass term \tilde{m}_z decreases as W_0 increases. When \tilde{m}_z reaches the critical point corresponding to $m_z = 2.5$ in Fig. 1(a), this trivial bulk gap closes and a pair of Weyl nodes emerge at the center of the Brillouin zone, realizing the phase transition from NI phase to DWSM phase. With further increasing of the disorder strength, the system evolves from DWSM phase to DM phase, and finally enters the AI phase. The global phase diagram in Fig. 2 is obtained by repeatedly calculating the normalized localization length and the Hall conductivity at various values of W_0 and m_z .

B. σ_x orbital disorder

There is another kind of disorder, i.e., the orbital disorder. The orbital disorder means that the electron could be randomly scattered from one orbital state to another orbital state. The σ_x term can also describe the spin-flip disorder [56]. This type of disorder exists widely and cannot be ignored when describing a real system, which has been investigated in previous research [47,56,57,71]. The research of the σ_x orbital disorder is missing in DWSM, which deserves to be studied in detail. Thus we next study the phase transition generated by σ_x orbital disorders. Figure 7 shows the global phase diagram for different m_z and disorder strengths W_x . Figures 8 and 9 give the typical results of the normalized localization length and the Hall conductivity for $m_z = 1.3, 1.48, 1.7$, and 2.2 .

Concerning the phase transition and for $m_z = 1.3$, as shown in Figs. 8(a) and 9(a), with increasing of the disorder strength W_x , the system also undergoes the phase transitions from 3D QAH to DM phase, which is similar with those given in Fig. 3(a) for the nonmagnetic disorder. For $m_z = 1.48$, the system is in the 3D QAH phase and close to the phase boundary of 3D QAH-DWSM [see Fig. 1(a)]. According to the results in Figs. 8(b) and 9(b), $d\Lambda/dL$ alters from a

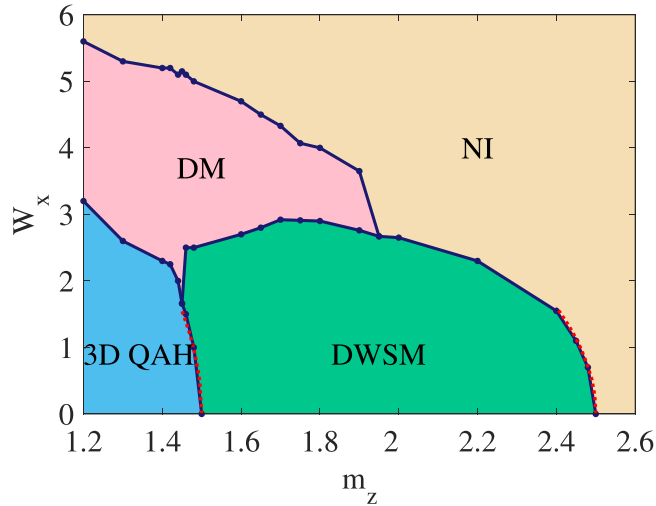


FIG. 7. Phase diagram on the W_x - m_z plane for $t_z = 0.5$ and $t_x = t_y = 1$. The dark blue solid lines with dots are identified by using the transfer matrix method. The accurate phases are determined by the Hall conductivity σ_{xy} . The red dotted line is obtained numerically from the SCBA method.

negative to positive value at $W_x=1$ and the Hall conductivity decreases from a quantized value $\sigma_{xy} = 16e^2/8h$ to $\sigma_{xy} = 14e^2/8h$, which demonstrates a transition from 3D QAH to DWSM phase. This result is consistent with previous study [47]. We use the zero-order BA to qualitatively explain this transition. In contrast with the nonmagnetic disorder that diminishes \tilde{m}_z , instead, according to Eq. (12), the σ_x orbital disorder has a positive correction to \tilde{m}_z . With increasing of the disorder strength W_x , \tilde{m}_z gradually increases and arrives at

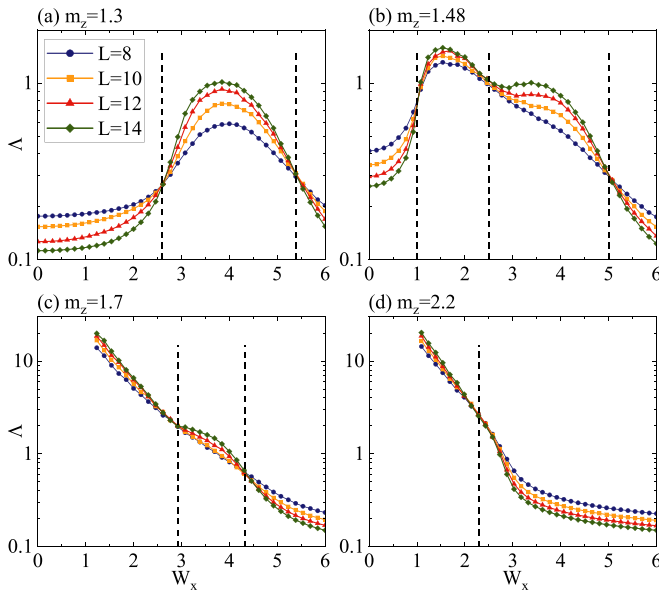


FIG. 8. The normalized localization length Λ is plotted as a function of the disorder strength W_x for the values of (a) $m_z = 1.3$, (b) 1.48, (c) 1.7, and (d) 2.2. Four colored curves are associated with different side lengths of the cross section. Other parameters are $t_z = 0.5$ and $t_x = t_y = 1$.

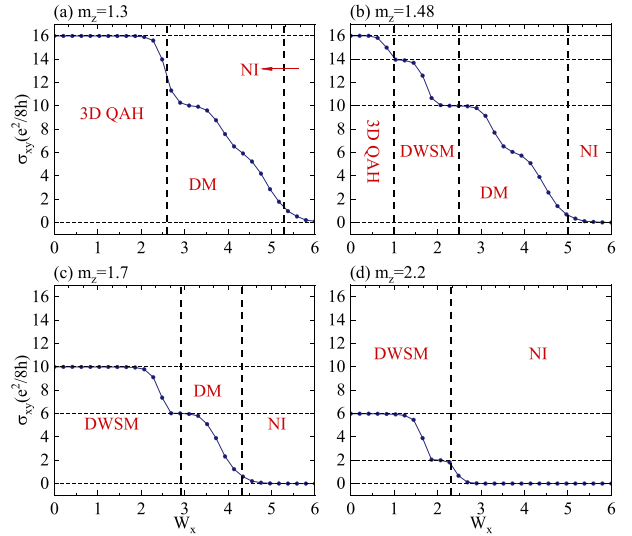


FIG. 9. The Hall conductivity σ_{xy} is plotted as a function of the disorder strength W_x for the values of (a) $m_z = 1.3$, (b) 1.48, (c) 1.7, and (d) 2.2. The system size is $40 \times 40 \times 8$. Other parameters are $t_z = 0.5$ and $t_x = t_y = 1$.

the value of 1.5, which is a phase boundary between 3D QAH and DWSM phase [see Fig. 1(a)]. The bulk gap closes and a pair of Weyl nodes emerge at the Brillouin zone boundary, inducing the 3D QAH–DWSM transition. Further increasing the disorder strength W_x , it can render the Weyl nodes to approach each other. The decrease of the distance between the Weyl nodes induces a plateau-to-plateau transition of the Hall conductivity from $\sigma_{xy} = 14e^2/8h$ to $\sigma_{xy} = 10e^2/8h$ [see Fig. 9(b)]. Note that the Hall conductivity of the system is proportional to the distance of two Weyl nodes. Subsequently, the system experiences the phase transition from DM to NI phase with increasing of W_x .

Likewise, the system undergoes the phase transitions from DWSM to DM phase, then to NI phase as the disorder strength W_x increases for the case $m_z = 1.7$, as shown in Figs. 8(c) and 9(c). This is similar to the result of the nonmagnetic disorder [see Fig. 4(c)].

For $m_z = 2.2$, the normalized localization length in Fig. 8(d) manifests the phase transition at $W_x = 2.3$. According to Fig. 9(d), the Hall conductivity varying from $2e^2/8h$ to zero demonstrates the DWSM–NI transition. This is a difference between the case of σ_0 and σ_x disorders. For σ_0 disorder, the system must undergo the DM phase before being localized by the strong disorder. However, the σ_x disorder generates a direct transition from DWSM to NI phase without going through the DM phase.

Figure 10 presents the DOS for the insulator phase at a fixed disorder strength $W_x = 5.5$ for different values of m_z . It is obvious that there exists a DOS gap with zero value in the energy range $-0.08 < E_f < 0.08$ eV [see Fig. 10(a)], in which the Hall conductivity becomes zero as shown in Figs. 9(c)–9(d). This means that, in the normal insulator phase, the Hall conductivity is zero, and DOS has zero value near the Fermi energy, while in the Anderson insulator phase, the Hall conductivity is also zero, but DOS has no zero value [see Figs. 4(c), 6(c)]. That is to say, the value of DOS is

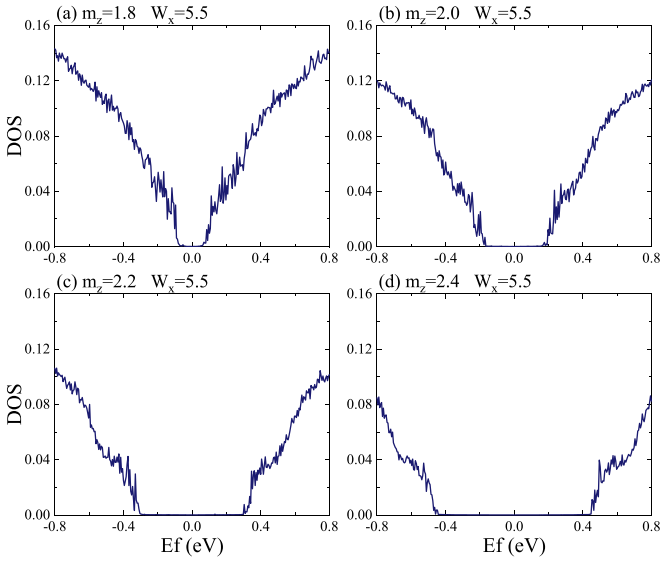


FIG. 10. DOS as a function of Fermi energy obtained by NEGF at $W_x = 5.5$ for (a) $m_z = 1.8$, (b) $m_z = 2.0$, (c) $m_z = 2.2$, and (d) $m_z = 2.4$. We can clearly see a gap near $E_f = 0$. Other parameters are $t_z = 0.5$ and $t_x = t_y = 1$.

crucial for us to distinguish the NI and AI phase when the Hall conductivity is zero. With increasing of m_z , the width of the DOS gap gradually increases from 0.16 to about 0.9, which associates with a more noticeable insulating state.

There is a prominent difference between σ_0 and σ_x disorders. When the system has a strong σ_0 disorder, the system enters the AI phase with a nonzero DOS [see Fig. 6(c)]. However, for σ_x disorder, the DOS in the normal insulator phase manifests that the system is a gapped insulator. These results indicate that these two kinds of disorders have an obviously different effect on the insulator phase of the system.

C. Combined effect of orbital disorders

In this section, we discuss the combined effect of three kinds of orbital disorders. Since σ_x and σ_y orbital disorders have identical correction to the mass term m_z , we take $W_x = W_y = W_{xy}$. We plot the phase diagrams on the W_z - W_{xy} plane for $m_z = 1.48$ (3D QAH phase in the clean system) in Fig. 11(a) and for $m_z = 1.52$ (DWSM phase in the clean system) in Fig. 11(b).

For $m_z = 1.48$, as shown in Fig. 11(a), when $W_{xy} < 0.73$, the system is first in 3D QAH phase, and then evolves into DM phase with increasing of W_z . When the disorder strength further increases, for example $W_{xy} = 0.95$ (see the blue vertical dashed line), the increase of W_z can induce the transition from DWSM to 3D QAH phase. We can interpret this phase transition according to the competition between W_{xy} and W_z . This competition can be illustrated according to Eq. (12). W_{xy} has positive correction to m_z while it is opposite for W_z . When $W_z < 0.7$, the renormalized mass term $\tilde{m}_z > 1.5$, so the system is still in DWSM phase. When W_z exceeds 0.7, the system enters the 3D QAH phase because the effect caused by W_z is greater than that of W_{xy} . The system goes into DM phase when W_z further increases and reaches the value of 2.5. When the disorder strength increases to $W_{xy} = 1.66$ (see the black

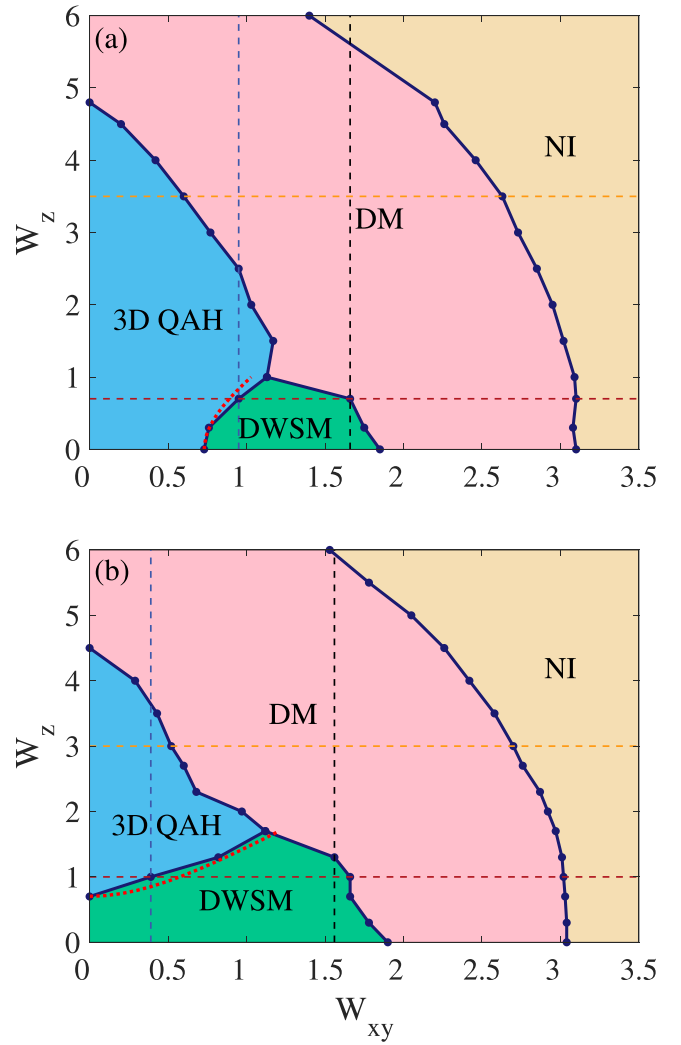


FIG. 11. Phase diagrams on the W_z - W_{xy} plane for (a) $m_z = 1.48$ and (b) $m_z = 1.52$. The dark blue solid lines with dots are identified by using the transfer matrix method. The accurate phases are determined by the Hall conductivity σ_{xy} . The red dotted line is obtained numerically from the SCBA method. Other parameters are $t_z = 0.5$ and $t_x = t_y = 1$.

vertical dashed line), the system undergoes the DWSM-DM-NI phase transitions. For $W_z = 0.7$ (see the red horizontal dashed line), when $W_{xy} > 0.95$, the system enters DWSM phase from 3D QAH phase because the effect of W_{xy} is greater than that of W_z . Further increasing W_{xy} can render the system evolve into DM and NI phase in sequence. For the case $W_z = 3.5$ (see the yellow horizontal dashed line), the system enters DM phase from 3D QAH phase when W_{xy} surpasses 0.6.

We can use the same competition between W_{xy} and W_z to describe the phase transition for the case $m_z = 1.52$, as shown in Fig. 11(b). For $W_{xy} = 0.39$ (see the blue vertical dashed line), the system experiences the DWSM-3D QAH-DM phase transitions with increasing of W_z . For $W_{xy} = 1.56$ (see the black vertical dashed line), the system undergoes the phase transition from DWSM to DM phase. For $W_z = 1.0$ (see the red horizontal dashed line), the system enters DWSM phase

from 3D QAH phase when W_{xy} exceeds 0.39. Then the system enters DM and NI phase with the increase of W_{xy} . For the case $W_z = 3.0$ (see the yellow horizontal dashed line), a 3D QAH-DM phase transition happens with increasing of W_{xy} , and then the system evolves into NI phase when W_{xy} exceeds the value of 2.76.

IV. SELF-CONSISTENT BORN APPROXIMATION

The self-consistent Born approximation is extensively used to analyze the weak-disorder effect in various systems [52,54,72]. In the SCBA framework, the disorder can generate a self-energy correction to the Hamiltonian and therefore renormalize the model parameters. The self-energy Σ can be calculated in terms of the following integral equation,

$$\Sigma = \frac{W^2}{12} \left(\frac{a}{2\pi} \right)^3 \int_{BZ} d^3k \{ \sigma_i [E - h(\mathbf{k}) - \Sigma]^{-1} \sigma_i \}, \quad (10)$$

where the self-energy can be written as $\Sigma = \Sigma_0 \sigma_0 + \Sigma_x \sigma_x + \Sigma_y \sigma_y + \Sigma_z \sigma_z$. The renormalized mass term is $\tilde{m}_z = m_z + \Sigma_z$. Next we introduce the numerical calculation method for SCBA. We use Eq. (10) to evaluate Σ_z . We transform the integral into the discrete summation

$$\Sigma_z = \frac{W^2}{12} \left(\frac{a}{2\pi} \right)^3 \sum_k \frac{d_z(k) + \Sigma_z}{\tilde{E}^2 - \sum_{\mu=1}^3 \tilde{d}_{\mu}^2(k)}. \quad (11)$$

The variable k is discrete with $k_{\alpha}^i = 2\pi n_i / N$; $n_i = 1, \dots, N$; $\alpha = x, y, z$; and $\Delta = 2\pi / N$. The iterative algorithm is listed as follows:

- (1) For a given m_z , choose a disorder strength W .
- (2) If it is the first iteration, set the initial value Σ_z^1 on the right-hand side of Eq. (11) to be zero. For the m th ($m \geq 2$) iteration, use Σ_z^{m-1} as the seed.
- (3) For each k_{α}^i , calculate $\frac{d_z(k_{\alpha}^i) + \Sigma_z^m}{\tilde{E}^2 - \sum_{\mu=1}^3 \tilde{d}_{\mu}^2(k_{\alpha}^i)} \Delta^3$ and add this term to the sum I_0 .
- (4) Repeat steps (2) and (3) until $|\Sigma_z^m - \Sigma_z^{m-1}| / |\Sigma_z^m| < \delta$.

In our calculation, we set $N = 400$ and $\delta = 0.001$. The results are plotted in the phase boundary of the phase diagrams with red dotted lines. The results obtained from SCBA are consistent with the results obtained from the transfer matrix method.

In order to qualitatively describe the phase transition, we can adopt the zero-order Born approximation by neglecting the Σ term on the right-hand side of Eq. (10), and obtain \tilde{m}_z with the zero-order correction

$$\tilde{m}_z = m_z + \frac{W^2 a^3}{192\pi^2} \int_{-\pi}^{\pi} \ln \left| \left(\frac{\pi}{a} \right)^4 \frac{8}{(k_z^2 + 4m_z - 10)^2} \right| dk_z, \quad (12)$$

with $W^2 = W_x^2 + W_y^2 - W_z^2 - W_0^2$. The detailed calculating steps are given in Appendix B. The integration on the right-hand side of Eq. (12) is always positive, so the σ_x orbital disorder W_x and σ_y orbital disorder W_y enlarge the value of \tilde{m}_z , while the on-site nonmagnetic disorder W_0 and σ_z orbital disorder W_z diminish \tilde{m}_z .

V. SUMMARY AND DISCUSSION

In summary, we first study the effect of the on-site nonmagnetic and orbital disorders in DWSM by calculating the localization length and the Hall conductivity. These disorders can give rise to rich phase transitions shown in the phase diagrams. First, the tight-binding Hamiltonian of DWSM is introduced in the momentum and real space. Then the phase diagram in the clean limit is presented. In the presence of the disorder, the results indicate that the 3D QAH phase and DWSM phase are stable in the weak disorder and the system undergoes a series of phase transitions with increasing of the disorder strength. For nonmagnetic disorder, phase transitions in DWSM are consistent with those reported in the Weyl semimetal [43,58]. We also calculate the DOS for different disorder strengths. For the σ_x orbital disorder, the 3D QAH-DWSM transition is also consistent with the previous research [47]. However, according to DOS calculation, the system enters the gapped insulator phase instead of the gapless AI phase which is generated by σ_0 disorder. Another difference is the direct transition from DWSM to NI phase, which is also different from the effect of the σ_0 disorder. For the latter, the system must enter the DM phase before being localized by the strong disorder. The combined effects of orbital disorders are also investigated for disordered 3D QAH and DWSM phases. Furthermore, the self-consistent Born approximation is introduced to explain the disorder-induced phase transitions. At last, we discuss the experimental realization of the disordered DWSM.

The DWSM is realized experimentally in photonic crystals by using planar fabrication technology with the robustness of the surface state [29]. Besides, the disorder-induced topological phase transition is observed experimentally from a trivial insulator to a topological Anderson insulator with robust chiral edge states [73]. The researchers fabricate a microwave-scale photonic crystal consisting of dielectric and gyromagnetic pillars. Disorder is introduced by randomly rotating the dielectric pillars in each unit cell, with the disorder strength parametrized by the maximum rotation angle. Therefore, we can utilize the same method to verify the disorder effect discussed in this article.

ACKNOWLEDGMENTS

We would like to thank Professor You-Quan Li (Zhejiang University) and Professor Pei Wang (Zhejiang Normal University) for helpful discussions. We thank the High-Performance Computing Platform of Hangzhou Dianzi University for providing computing resources, and this work was supported by the National Natural Science Foundation of China (Grant No. 11574067).

APPENDIX A: CALCULATION OF DENSITY OF STATES

In this Appendix, we show the DOS calculation by using the NEGF method [19,74]. The DOS is expressed as

$$\rho(E) = -\frac{1}{\pi L_x L_y L_z} \text{Im}[\text{Tr}(G^r)]. \quad (A1)$$

L_x , L_y , and L_z are the system size along the x , y , z directions. G^r is the retarded Green's function of the system. We utilize the following algorithm to calculate the retarded Green's

function G^r :

$$G_{ii}^r = [E - H_{ii} - H_{i,i-1} G_{i-1,i-1}^{r,R(i-1)} H_{i-1,i} - H_{i,i+1} G_{i+1,i+1}^{r,L(i+1)} H_{i+1,i}]^{-1}, \quad (\text{A2})$$

$$G_{ii}^{r,R(i)} = [E - H_{ii} - H_{i,i-1} G_{i-1,i-1}^{r,R(i-1)} H_{i-1,i}]^{-1}, \quad (\text{A3a})$$

$$G_{ii}^{r,L(i)} = [E - H_{ii} - H_{i,i+1} G_{i+1,i+1}^{r,L(i+1)} H_{i+1,i}]^{-1}. \quad (\text{A3b})$$

In the above formulas, G_{ii}^r is the i th slice's Green's function of the whole system. $G_{ii}^{r,R(L)(i)}$ is the i th slice's Green's function of the first i slices ($i < L_z$). R (L) means the iteration is along the z ($-z$) direction. All the diagonal elements of the retarded Green's function of the system G_{ii}^r can be evaluated. Then the DOS of the system is

$$\rho(E) = -\frac{1}{\pi L_x L_y L_z} \sum_{i=1}^{L_z} \text{Im}[\text{Tr}(G_{ii}^r)]. \quad (\text{A4})$$

APPENDIX B: BORN APPROXIMATION

In this Appendix, we give the detailed calculating process of the self-energy, which is given by

$$\Sigma = \frac{W_0^2}{12} \left(\frac{a}{2\pi}\right)^3 \int_{BZ} dk^3 \{\sigma_i [E - h(\mathbf{k}) - \Sigma]^{-1} \sigma_i\}. \quad (\text{B1})$$

The self-energy and the Hamiltonian can be expressed with Pauli matrices

$$\Sigma = \Sigma_0 \sigma_0 + \Sigma_x \sigma_x + \Sigma_y \sigma_y + \Sigma_z \sigma_z, \quad (\text{B2a})$$

$$h(\mathbf{k}) = d_0 \sigma_0 + d_x \sigma_x + d_y \sigma_y + d_z \sigma_z. \quad (\text{B2b})$$

We substitute these terms into Eq. (B1),

$$[E - h(\mathbf{k}) - \Sigma]^{-1} = \frac{\tilde{E} + \sum_{\mu} \tilde{d}_{\mu} \sigma_{\mu}}{\tilde{E}^2 - \sum_{\mu} \tilde{d}_{\mu}^2}, \quad (\text{B3})$$

where

$$E - h(\mathbf{k}) - \Sigma = E - \sum_{\mu} d_{\mu} \sigma_{\mu} - \sum_{\mu} \Sigma_{\mu} \sigma_{\mu} = \tilde{E} - \sum_{\mu} \tilde{d}_{\mu} \sigma_{\mu},$$

with $\tilde{E} = E - (d_0 + \Sigma_0)$ and $\tilde{d}_{\mu} = d_{\mu} + \Sigma_{\mu}$. To simplify we only discuss σ_0 disorder. Substituting Eq. (B3) into Eq. (B1), we can obtain the z component of the self-energy

$$\Sigma_z = \frac{W_0^2}{12} \left(\frac{a}{2\pi}\right)^3 \int_{BZ} d^3 k \frac{d_z + \Sigma_z}{\tilde{E}^2 - \sum_{\mu} \tilde{d}_{\mu}^2}. \quad (\text{B4})$$

We expand the Hamiltonian at $(0,0,0)$ to k^2 order,

$$h_1(\mathbf{k}) \approx \frac{1}{2} (k_y^2 - k_x^2) \sigma_x + k_x k_y \sigma_y + \left[m_z + \frac{1}{4} (2k_y^2 + 2k_x^2 + k_z^2) - \frac{5}{2} \right], \quad (\text{B5})$$

and substitute $h_1(\mathbf{k})$ into Eq. (B4). In order to get the zero-order Born approximation, we need to neglect the Σ_z term on the right-hand side of Eq. (B4). Then we get the integral expression

$$\Sigma_z = -\frac{W_0^2}{12} \left(\frac{a}{2\pi}\right)^3 \int d^3 k \frac{m_z + \frac{1}{2} (k_x^2 + k_y^2) + \frac{1}{4} k_z^2 - \frac{5}{2}}{\frac{1}{4} (k_y^2 - k_x^2)^2 + (k_x k_y)^2 + [m_z + \frac{1}{2} (k_x^2 + k_y^2) + \frac{1}{4} k_z^2 - \frac{5}{2}]^2}. \quad (\text{B6})$$

The integrand only depends on k^2 , so we can transform it to polar coordinates, namely $\int d^2 k = \int d\theta \int k dk = 2\pi \int k dk$. By using this transformation, Σ_z can be further simplified as

$$\Sigma_z = -\frac{W_0^2 a^3}{48\pi^2} \int dk_z \int 2\pi dk_{//} \frac{k_{//}^3 + 2\lambda(k_z) k_{//}}{k_{//}^4 + 2\lambda^2(k_z) + 2\lambda(k_z) k_{//}},$$

with

$$\lambda(k_z) = \frac{1}{4} k_z^2 + m_z - \frac{5}{2}.$$

The integral we need to solve is of the form

$$\int_0^{\Lambda} dk \frac{Ak - k^3}{B + ck^2 + k^4} \approx -\frac{1}{4} \ln \left| \frac{\Lambda^4}{B} \right|,$$

with $\Lambda = \pi/a$. Eventually we obtain the zero-order Born approximation expression

$$\Sigma_z = -\frac{W_0^2 a^3}{192\pi^2} \int_{-\pi}^{\pi} \ln \left| \left(\frac{\pi}{a}\right)^4 \frac{8}{(k_z^2 + 4m_z - 10)^2} \right| dk_z. \quad (\text{B7})$$

This integral is difficult to be further calculated analytically, so we use this expression to qualitatively analyze the disorder effect.

- [1] M. Z. Hasan, S. Y. Xu, I. Belopolski, and S. M. Huang, *Annu. Rev. Condens. Matter Phys.* **8**, 289 (2017).
- [2] N. P. Armitage, E. J. Mele, and A. Vishwanath, *Rev. Mod. Phys.* **90**, 015001 (2018).
- [3] M. Z. Hasan, G. Chang, I. Belopolski, Ilya Belopolski, Guang Bian, S. Y. Xu, and J. X. Yin, *Nat. Rev. Mater.* **6**, 784 (2021).
- [4] X. Wan, A. M. Turner, A. Vishwanath, and S. Y. Savrasov, *Phys. Rev. B* **83**, 205101 (2011).

- [5] D. Bulmash, C. X. Liu, and X. L. Qi, *Phys. Rev. B* **89**, 081106(R) (2014).
- [6] G. Xu, H. Weng, Z. Wang, X. Dai, and Z. Fang, *Phys. Rev. Lett.* **107**, 186806 (2011).
- [7] J. Liu and D. Vanderbilt, *Phys. Rev. B* **90**, 155316 (2014).
- [8] S. M. Huang, S. Y. Xu, I. Belopolski, C. C. Lee, G. Chang, B. Wang, N. Alidoust, G. Bian, M. Neupane, C. Zhang, S. Jia, A. Bansil, H. Lin, and M. Z. Hasan, *Nat. Commun.* **6**, 7373 (2015).

- [9] H. Weng, C. Fang, Z. Fang, B. A. Bernevig, and X. Dai, *Phys. Rev. X* **5**, 011029 (2015).
- [10] S. Y. Xu, I. Belopolski, N. Alidoust, M. Neupane, G. Bian, C. Zhang, R. Sankar, G. Chang, Z. Yuan, C. C. Lee, S. M. Huang, H. Zheng, J. Ma, D. S. Sanchez, B. Wang, A. Bansil, F. Chou, P. P. Shibayev, H. Lin, S. Jia, and M. Zahid Hasan, *Science* **349**, 613 (2015); B. Q. Lv, N. Xu, H. M. Weng, J. Z. Ma, P. Richard, X. C. Huang, L. X. Zhao, G. F. Chen, C. E. Matt, F. Bisti, V. N. Strocov, J. Mesot, Z. Fang, X. Dai, T. Qian, M. Shi, and H. Ding, *Nat. Phys.* **11**, 724 (2015); L. X. Yang, Z. K. Liu, Y. Sun, H. Peng, H. F. Yang, T. Zhang, B. Zhou, Y. Zhang, Y. F. Guo, M. Rahn, D. Prabhakaran, Z. Hussain, S. K. Mo, C. Felser, B. Yan, and Y. L. Chen, *ibid.* **11**, 728 (2015).
- [11] N. Morali, R. Batabyal, P. K. Nag, E. Liu, Q. Xu, Y. Sun, B. Yan, C. Felser, N. Avraham, and H. Beidenkopf, *Science* **365**, 1286 (2019).
- [12] K. Deng, G. Wan, P. Deng, K. Zhang, S. Ding, E. Wang, M. Yan, H. Huang, H. Zhang, Z. Xu, J. Denlinger, A. Fedorov, H. Yang, W. Duan, H. Yao, Y. Wu, S. Fan, H. Zhang, X. Chen, and S. Zhou, *Nat. Phys.* **12**, 1105 (2016).
- [13] H. B. Nielsen and M. Ninomiya, *Phys. Lett. B* **130**, 389 (1983).
- [14] X. Huang, L. Zhao, Y. Long, P. Wang, D. Chen, Z. Yang, H. Liang, M. Xue, H. Weng, Z. Fang, X. Dai, and G. Chen, *Phys. Rev. X* **5**, 031023 (2015).
- [15] A. A. Zyuzin and A. A. Burkov, *Phys. Rev. B* **86**, 115133 (2012).
- [16] C. L. Zhang, S. Y. Xu, I. Belopolski, Z. Yuan, Z. Lin, B. Tong, G. Bian, N. Alidoust, C. C. Lee, S. M. Huang, T. R. Chang, G. Chang, C. H. Hsu, H. T. Jeng, M. Neupane, D. S. Sanchez, H. Zheng, J. Wang, H. Lin, C. Zhang *et al.*, *Nat. Commun.* **7**, 10735 (2016).
- [17] J. H. Zhou, H. Jiang, Q. Niu, and J. R. Shi, *Chin. Phys. Lett.* **30**, 027101 (2013).
- [18] C. M. Wang, H. P. Sun, H. Z. Lu, and X. C. Xie, *Phys. Rev. Lett.* **119**, 136806 (2017).
- [19] H. Li, H. Liu, H. Jiang, and X. C. Xie, *Phys. Rev. Lett.* **125**, 036602 (2020).
- [20] F. Tang, Y. Ren, P. Wang, R. Zhong, J. Schneeloch, S. A. Yang, K. Yang, P. A. Lee, G. Gu, Z. Qiao, and L. Zhang, *Nature (London)* **569**, 537 (2019).
- [21] E. Liu, Y. Sun, N. Kumar, L. Muechler, A. Sun, L. Jiao, S. Y. Yang, D. Liu, A. Liang, Q. Xu, J. Kroder, V. Süß, H. Borrmann, C. Shekhar, Z. Wang, C. Xi, W. Wang, W. Schnelle, S. Wirth, Y. Chen *et al.*, *Nat. Phys.* **14**, 1125 (2018).
- [22] T. Liang, J. Lin, Q. Gibson, S. Kushwaha, M. Liu, W. Wang, H. Xiong, J. A. Sobota, M. Hashimoto, P. S. Kirchmann, Z. X. Shen, R. J. Cava, and N. P. Ong, *Nat. Phys.* **14**, 451 (2018).
- [23] T. Morimoto and N. Nagaosa, *Sci. Adv.* **2**, e1501524 (2016).
- [24] L. Wu, S. Patankar, T. Morimoto, N. L. Nair, E. Thewalt, A. Little, J. G. Analytis, J. E. Moore, and J. Orenstein, *Nat. Phys.* **13**, 350 (2017).
- [25] S. Polatkan, M. O. Goerbig, J. Wyzula, R. Kemmler, L. Z. Maulana, B. A. Piot, I. Crassee, A. Akrap, C. Shekhar, C. Felser, M. Dressel, A. V. Pronin, and M. Orlita, *Phys. Rev. Lett.* **124**, 176402 (2020).
- [26] Y. Okamura, S. Minami, Y. Kato, Y. Fujishiro, Y. Kaneko, J. Ikeda, J. Muramoto, R. Kaneko, K. Ueda, V. Kocsis, N. Kanazawa, Y. Taguchi, T. Koretsune, K. Fujiwara, A. Tsukazaki, R. Arita, Y. Tokura, and Y. Takahashi, *Nat. Commun.* **11**, 4619 (2020).
- [27] C. Fang, M. J. Gilbert, X. Dai, and B. A. Bernevig, *Phys. Rev. Lett.* **108**, 266802 (2012).
- [28] S. M. Huang, S. Y. Xu, I. Belopolski, C. C. Lee, G. Chang, T. R. Chang, B. Wang, N. Alidoust, G. Bian, M. Neupane, D. Sanchez, H. Zheng, H. T. Jeng, A. Bansil, T. Neupert, H. Lin, and M. Z. Hasan, *Proc. Natl. Acad. Sci. U.S.A.* **113**, 1180 (2016).
- [29] W. J. Chen, M. Xiao, and C. T. Chan, *Nat. Commun.* **7**, 13038 (2016).
- [30] S. Ahn, E. J. Mele, and H. Min, *Phys. Rev. B* **95**, 161112(R) (2017).
- [31] M. Umer, R. W. Bomantara, and J. Gong, *J. Phys. Mater.* **4**, 045003 (2021).
- [32] X. Y. Mai, D. W. Zhang, Z. Li, and S. L. Zhu, *Phys. Rev. A* **95**, 063616 (2017).
- [33] R. M. A. Dantas, F. Pena-Benitez, B. Roy, and P. Surg'wka, *Phys. Rev. Res.* **2**, 013007 (2020).
- [34] P. W. Anderson, *Phys. Rev.* **109**, 1492 (1958).
- [35] J. Li, R. L. Chu, J. K. Jain, and S. Q. Shen, *Phys. Rev. Lett.* **102**, 136806 (2009).
- [36] H. M. Guo, G. Rosenberg, G. Refael, and M. Franz, *Phys. Rev. Lett.* **105**, 216601 (2010).
- [37] C. P. Orth, T. Sekera, C. Bruder, and T. L. Schmidt, *Sci. Rep.* **6**, 24007 (2016).
- [38] H. Jiang, L. Wang, Q. F. Sun, and X. C. Xie, *Phys. Rev. B* **80**, 165316 (2009).
- [39] C. Z. Chen, H. W. Liu, H. Jiang, Q. F. Sun, Z. Q. Wang, and X. C. Xie, *Phys. Rev. B* **91**, 214202 (2015).
- [40] R. Chen, D. H. Xu, and B. Zhou, *Phys. Rev. B* **95**, 245305 (2017).
- [41] R. Chen, D. H. Xu, and B. Zhou, *Phys. Rev. B* **100**, 115311 (2019).
- [42] T. Peng, C. B. Hua, R. Chen, D. H. Xu, and B. Zhou, *Phys. Rev. B* **103**, 085307 (2021).
- [43] H. Shapourian and T. L. Hughes, *Phys. Rev. B* **93**, 075108 (2016).
- [44] Y. Su, X. S. Wang, and X. R. Wang, *Sci. Rep.* **7**, 14382 (2017).
- [45] Y. J. Wu, H. W. Liu, H. Jiang, and X. C. Xie, *Phys. Rev. B* **96**, 024201 (2017).
- [46] M. Trescher, B. Sbierski, P. W. Brouwer, and E. J. Bergholtz, *Phys. Rev. B* **95**, 045139 (2017).
- [47] R. Chen, C. Z. Chen, J. H. Sun, B. Zhou, and D. H. Xu, *Phys. Rev. B* **97**, 235109 (2018).
- [48] S. Bera, J. D. Sau, and B. Roy, *Phys. Rev. B* **93**, 201302(R) (2016).
- [49] Y. S. Hu, Y. R. Ding, J. Zhang, Z. Q. Zhang, and C. Z. Chen, *Phys. Rev. B* **104**, 094201 (2021).
- [50] Z. Q. Zhang, B. L. Wu, C. Z. Chen, and H. Jiang, *Phys. Rev. B* **104**, 014203 (2021).
- [51] M. J. Park, B. Basa, and M. J. Gilbert, *Phys. Rev. B* **95**, 094201 (2017).
- [52] J. T. Song, H. W. Liu, H. Jiang, Q. F. Sun, and X. C. Xie, *Phys. Rev. B* **85**, 195125 (2012).
- [53] E. J. Meier, F. A. An, A. Dauphin, M. Maffei, P. Massignan, T. L. Hughes, and B. Gadway, *Science* **362**, 929 (2018).
- [54] H. H. Hung, A. Barr, E. Prodan, and G. A. Fiete, *Phys. Rev. B* **94**, 235132 (2016).
- [55] L. H. Hu, D. H. Xu, F. C. Zhang, and Y. Zhou, *Phys. Rev. B* **94**, 085306 (2016).

- [56] Z. Qiao, Y. Han, L. Zhang, K. Wang, X. Deng, H. Jiang, S. A. Yang, J. Wang, and Q. Niu, *Phys. Rev. Lett.* **117**, 056802 (2016).
- [57] H. Yang, J. J. Zeng, Y. L. Han, and Z. H. Qiao, *Phys. Rev. B* **104**, 115414 (2021).
- [58] C. Z. Chen, J. Song, H. Jiang, Q. F. Sun, Z. Wang, and X. C. Xie, *Phys. Rev. Lett.* **115**, 246603 (2015).
- [59] Q. Liu, C. X. Liu, C. K. Xu, X. L. Qi, and S. C. Zhang, *Phys. Rev. Lett.* **102**, 156603 (2009).
- [60] F. Milde, Ph.D. thesis, Technischen Universität Chemnitz, 2000.
- [61] A. MacKinnon and B. Kramer, *Phys. Rev. Lett.* **47**, 1546 (1981).
- [62] A. MacKinnon and B. Kramer, *Z. Phys. B* **53**, 1 (1983).
- [63] B. Kramer and A. MacKinnon, *Rep. Prog. Phys.* **56**, 1469 (1993).
- [64] K. Slevin and T. Ohtsuki, *New J. Phys.* **16**, 015012 (2014).
- [65] A. A. Burkov and L. Balents, *Phys. Rev. Lett.* **107**, 127205 (2011).
- [66] E. Prodan, *J. Phys. A: Math. Theor.* **44**, 113001 (2011).
- [67] E. Prodan, T. L. Hughes, and B. A. Bernevig, *Phys. Rev. Lett.* **105**, 115501 (2010).
- [68] E. Prodan, *Phys. Rev. B* **83**, 195119 (2011).
- [69] Z. X. Su, Y. Z. Kang, B. F. Zhang, Z. Q. Zhang, and H. Jiang, *Chin. Phys. B* **28**, 117301 (2019).
- [70] Y. Wang, *Europhys. Lett.* **126**, 67005 (2019).
- [71] H. Li, Hua Jiang, C. Z. Chen, and X. C. Xie, *Phys. Rev. Lett.* **126**, 156601 (2021).
- [72] C. W. Groth, M. Wimmer, A. R. Akhmerov, J. Tworzydło, and C. W. J. Beenakker, *Phys. Rev. Lett.* **103**, 196805 (2009).
- [73] G. G. Liu, Y. Yang, X. Ren, H. Xue, X. Lin, Y. H. Hu, H. X. Sun, B. Peng, P. Zhou, Y. Chong, and B. Zhang, *Phys. Rev. Lett.* **125**, 133603 (2020).
- [74] D. A. Ryndyk, *Theory of Quantum Transport at Nanoscale: An Introduction* (Springer, Dresden, 2016).